

Coherent control of bond making: The performance of rationally phase-shaped femtosecond laser pulses*

Liat Levin,¹ Wojciech Skomorowski,² Ronnie Kosloff,³ Christiane P. Koch,² and Zohar Amitay¹

¹*The Shirlee Jacobs Femtosecond Laser Research Laboratory,*

Schulich Faculty of Chemistry, Technion-Israel Institute of Technology, Haifa 32000, Israel

²*Theoretische Physik, Universität Kassel, Heinrich-Plett-Straße 40, 34132 Kassel, Germany*

³*Fritz Haber Research Centre and The Department of Physical Chemistry, Hebrew University, Jerusalem 91904, Israel*

(Dated: August 14, 2021)

The first step in the coherent control of a photoinduced binary reaction is bond making or photoassociation. We have recently demonstrated coherent control of bond making in multi-photon femtosecond photoassociation of hot magnesium atoms, using linearly chirped pulses [Levin et al., arXiv:1411.1542]. The detected yield of photoassociated magnesium dimers was enhanced by positively chirped pulses which is explained theoretically by a combination of purification and chirp-dependent Raman transitions. The yield could be further enhanced by pulse optimization resulting in pulses with an effective linear chirp and a sub-pulse structure, where the latter allows for exploiting vibrational coherences. Here, we systematically explore the efficiency of phase-shaped pulses for the coherent control of bond making, employing a parametrization of the spectral phases in the form of cosine functions. We find up to an order of magnitude enhancement of the yield compared to the unshaped transform-limited pulse. The highly performing pulses all display an overall temporally increasing instantaneous frequency and are composed of several overlapping sub-pulses. The time delay between the first two sub-pulses almost perfectly fits the vibrational frequency of the generated intermediate wavepacket. These findings are in agreement with chirp-dependent Raman transitions and exploitation of vibrational dynamics as underlying control mechanisms.

PACS numbers: 42.65.Re, 82.50.Nd, 82.53.Eb, 82.53.Kp

I. INTRODUCTION

Quantum coherent control of photo-induced processes [1–3] directs a quantum system from its initial state to desired final state(s) by manipulating interferences among coherent excitation pathways. When using strong femtosecond laser pulses, control can be realized—based on the broad spectrum, high intensity and ultrashort duration of the pulses—by tailoring their temporal shape [4]. Coherent control using tailored short pulses is nowadays successfully employed in many different areas of quantum physics, including photoionization and fragmentation, nuclear magnetic resonance and quantum information processing. However, the dream of coherently controlling photo-induced bimolecular chemical reactions [1, 5–7] which was at the origin of coherent control, still stands open. For example, it is not yet understood under which conditions a bimolecular reaction can be controlled and which reaction mechanisms are particularly susceptible to control. This dream has attracted significant interest over the years including that of Moshe Shapiro [6–10] since it holds the promise of creating a new type of photochemistry.

Two possible scenarios for the coherent control of a bimolecular reaction have been discussed in the literature. The first one relies on preparing coherent superposition states, in order to determine the outcome of the reaction [8–10]. Realizing this scenario requires control over reactive collisions which currently seems to be extremely challenging. Given, however, recent advances with cold [11, 12] and ultracold molecules [13], we may witness the advent of such a coherent chemistry in the not too distant future.

The second scenario utilizes interference in time rather than frequency domain, i.e., it is built on short, shaped pulses to induce bond making (photoassociation) and breaking (photodissociation) [14]. The coherence of the reactants required for controlling bond making must then be prepared during the photo-induced process. This is the reason why coherent control of a binary reaction has proven so difficult. The quantumness of an ensemble of reaction partners can be measured in terms of the purity, $\mathcal{P} = \text{Tr}[\rho^2]$, where ρ describes the state of the reaction partners, initially a thermal ensemble, $\rho_0 \sim \exp[-H/k_B T]$. Note that the purity is closely related to the entropy of the sample; and thus the coherent interaction of the reaction partners with the laser light does not change the purity. Preparation of coherence can still be achieved by addressing a subensemble of reactants. One possibility is given by filtering

*dedicated to the memory of Moshe Shapiro

out collision pairs in a small Franck-Condon window close to the repulsive barrier of the potential, as demonstrated by us in multi-photon femtosecond photoassociation of hot magnesium atoms [15]. The selected collision pairs are correlated due to the strong interaction close to the barrier. Correspondingly, the subensemble of photoassociated, electronically excited molecules shows coherent transient vibrational and rotational dynamics that were identified using pump-probe femtosecond spectroscopy [15]. The generation of molecular coherence was shown to be possible, even though the thermal ensemble of atoms was completely incoherent, with an initial purity of essentially zero. The generated coherences are amenable to coherent control, as demonstrated by us very recently [16]: The yield of detected magnesium dimers is enhanced by positively chirped pulses and suppressed by negatively chirped pulses. Our *ab initio* model has revealed that control is achieved by purification combined with chirp-dependent Raman transitions. Then, in closed-loop optimization experiments, an improved pulse was obtained that displays an effective temporal linear chirp and is composed of two sub-pulses. The latter allows for utilizing coherent vibrational dynamics in addition to the chirp-dependent Raman transitions [16].

Here, we utilize the insight gained earlier [16] and demonstrate an even higher degree of coherent control over bond making in femtosecond photoassociation of hot magnesium atoms, achieving up to an order-of-magnitude enhancement of the yield compared to the unshaped transform-limited pulse. The highly performing phase-shaped pulses all display an overall temporally increasing instantaneous frequency and are composed of several overlapping sub-pulses, where the time separation between the first two sub-pulses almost perfectly fits the vibrational frequency of the generated intermediate wavepacket. The corresponding spectral phases have the general form of a cosine function. These findings can again be rationalized by chirp-dependent Raman transitions and exploitation of vibrational dynamics as underlying control mechanisms.

II. EXCITATION SCHEME AND CONTROL SIGNATURE

Pairs of magnesium atoms are photoexcited to form a magnesium dimer, $\text{Mg} + \text{Mg} \rightarrow \text{Mg}_2^*$. Figure 1 presents the bond-making excitation scheme, starting from the van der Waals ground electronic state, $X^1\Sigma_g^+$, and using a non-resonant two-photon transition to the $(1)\Pi_g$ as a first step [15]. Initially, the magnesium atoms, held at a temperature of 1000 K, thermally populate a manifold of X -state scattering states, indicated by the blue-shaded area in Fig. 1. The excitation is driven by a strong, linearly polarized, shaped femtosecond pulse, characterized by a transform-limited

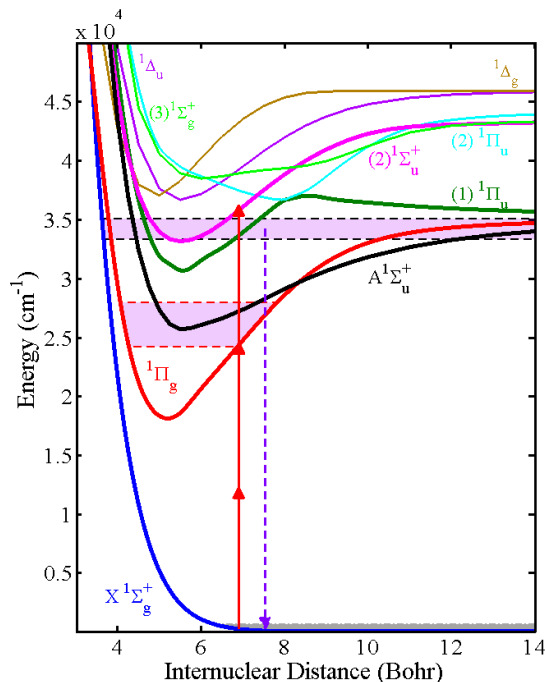


FIG. 1: The bond-making excitation scheme and potential energy curves of the magnesium dimer. The excitation by three NIR photons is indicated by the red arrows and the UV emission by the dashed purple arrow. The shaded areas show the thermally populated X -state scattering states as well as the band of rovibrational levels after two-photon excitation and that from which UV emission is observed.

(TL) duration of 70 fs and a central wavelength of 840 nm. The pulse energy corresponds to a TL peak intensity of 7.2×10^{12} W/cm². Following the irradiation, atom pairs with short internuclear separation undergo bond formation via a free-to-bound transition into bound levels of a manifold of electronically excited states of Mg₂. The gateway for this excitation is the excited state $(1)^1\Pi_g$, and the corresponding range of rovibrational levels that are populated in the $^1\Pi_g$ state is indicated in Fig. 1 (in-between red dashed lines).

The photoassociated molecules are detected by measuring the intensity of their UV fluorescence back to the ground electronic state, with a lifetime of a few ns, in the wavelength range of 285-292 nm. This corresponds to UV emission from below the atomic asymptote $^1P + ^1S$ of excited Mg atoms (see the dashed blue arrow schematically shown in Fig. 1). The corresponding range of UV-emitting levels which belong to the $A^1\Sigma_u^+$, $(1)^1\Pi_u$, and $(2)^1\Sigma_u^+$ electronically excited states, is also indicated in Fig. 1 (in-between dashed black lines).

The total UV signal originates from an incoherent summation over the signals obtained for all thermally populated initial scattering states which are characterized by their angular momentum J and collision energy E_{coll} . We have previously shown [15, 17] that the main contribution to the signal is from high partial waves, with J around 70, where due to the centrifugal barrier the shallow van-der-Waals potential well of the X-state supports only very few bound levels or no bound levels at all. This also implies that, as we have calculated [17], the bound-bound contribution to our signal corresponding to excitation from bound levels in the X-state amounts to less than 20% of our total signal.

The bond-making excitation is controlled using phase-shaped femtosecond pulses. Our earlier study [16] employed pulses with a linear chirp having a spectral phase of the form $\Phi(\omega) = \frac{1}{2}k(\omega - \omega_0)^2$, where ω_0 is the central frequency and k is the linear chirp parameter. The best linearly chirped pulse, with $k = 0.006$ ps², enhances the UV signal, compared to the TL pulse, by a factor of 5.4. Closed-loop optimization experiments have led to an improved pulse, yielding an enhancement factor of 7.4, which features an effective temporal linear chirp and is composed of two sub-pulses. Here, we investigate two additional sets of shaped pulses, all having a cosine spectral phase of the form

$$\Phi(\omega) = A \cos[(\omega - \omega_0)T + M], \quad (1)$$

characterized by three parameters, A , T and M . Such a spectral phase temporally yields a sequence of sub-pulses with a constant time difference T between subsequent sub-pulses. Once the value of T is smaller than or comparable to the TL pulse duration, 70 fs in our case, the overall pulse results from several overlapping sub-pulses that interfere with each other. Hence, with $M=0$, and A and T having appropriate values, the spectral phase of Eq. (1) results in a pseudo-chirped pulse. Such a pulse has a symmetric temporal intensity profile with no splitting into separated sub-pulses. It therefore can be assigned a well-defined pulse duration calculated as its full width at half maximum. At the same time, during the pulse's main intensity peak, the instantaneous temporal frequency increases, respectively decreases, monotonically. Hence, a pseudo-chirped pulse can be characterized by pulse duration and slope of the instantaneous frequency. Examples of pseudo-chirped pulses are shown below in Fig. 2(a)-(f). For a given bandwidth, a set of such pulses includes more combinations of pulse duration and instantaneous frequency slope than a set of linearly chirped pulses. This allows for a systematic investigation of the interplay of chirp-dependent Raman transitions and exploitation of vibrational coherence by temporally spaced pulses, and is the first set of pulses we employ here.

The second set of shaped pulses we utilize has cosine spectral phases with $M = 5.7$. With an additional proper choice for the values of A and T , the resulting shaped pulses are asymmetric in time and effectively composed of several, partially overlapping sub-pulses. Each sub-pulse has its own intensity and width, and the time difference between subsequent sub-pulses can change across the complete sequence. These shaped pulses also exhibit an instantaneous frequency that overall increases, respectively decreases, in time. Examples of these asymmetric pulses are found below in Fig. 4(a)-(f). For a given bandwidth, this set of pulses allows for a systematic investigation of the role of the time delay between the sub-pulses as well as their relative intensity.

III. EXPERIMENTAL DETAILS AND THEORETICAL MODEL

The magnesium photoassociation experiments are conducted in a heat pipe with Ar buffer gas heated to 1000 K, in which the pressure of the Mg vapor is around 5 Torr. Although a buffer gas is needed for the stable and continuous operation of the heated cell over long time, it does not play a part in the reaction. This is confirmed by observation of a UV signal even without the buffer gas. Furthermore, the observed UV signal remains the same when replacing argon with helium as a buffer gas. As we have previously discussed [16], the UV signal can be ruled out to result from Mg ionization [18]. Past experimental work shows that the existence of Mg clusters larger than a dimer is highly negligible in our heat pipe [19]. We therefore conclude that our measured signal results only from excitation of magnesium dimers.

The shaped femtosecond laser pulses irradiate the sample at a repetition rate of 1 kHz, after undergoing shaping using a liquid-crystal spatial light phase modulator [20]. The measured UV fluorescence signal is collected at the laser

beam entrance to the heat pipe, at a small angle from the beam axis, using a dichroic mirror, filter and lens, focusing the UV light onto an optical fiber that is coupled to a spectrometer and a time-gated camera system with a 5 ns gate.

We employ the theoretical framework developed in Refs. [15–17, 21] to describe photoassociation of hot atoms by an intense laser field. Our first principles model combines *ab initio* electronic structure theory for the Mg_2 molecule with quantum molecular dynamics to describe the light-matter interaction in a non-perturbative way. Random phase wavefunctions are employed to account for thermal averaging [17]. In brief, we explicitly include all electronic states shown in Fig. 1. The $X^1\Sigma_g^+$ ground electronic state is coupled to the $(1)^1\Pi_g$ state by a two-photon coupling. Then, the $(1)^1\Pi_g$ state is coupled by resonant one-photon couplings with a several states of *ungerade* symmetry, the most important of which are $A^1\Sigma_u^+$, $(1)^1\Pi_u$ and $(2)^1\Sigma_u^+$. In addition, there are near-resonant one-photon couplings with the $^1\Delta_{u/g}$ states. Moreover, since the system is exposed to a strong field, we also include the Stark shifts due to one-photon couplings with off-resonant states. The strong nonadiabatic interaction between the first two $^1\Pi_u$ states is taken into account by transformation into the diabatic basis. The general structure of the Hamiltonian is given in Eq. (12) of Ref. [17]; it is augmented here by the additional states shown in Fig. 1 and their one-photon couplings to the $(1)^1\Pi_g$ state. The time-dependent Schrödinger equation is solved using the Chebyshev propagator [22] separately for each thermal random-phase basis wavefunction and rotational quantum number J [17]. Any coupling between rotational and vibrational degrees of freedom is neglected to ease the computational effort. Time-dependent, thermally averaged expectation values are calculated by proper weighting for each partial wave, cf. Eqs. (25) and (26) of Ref. [17]. When the propagation is over, the final populations of the bound levels in the $A^1\Sigma_u^+$, $(1)^1\Pi_u$ and $(2)^1\Sigma_u^+$ excited states are used to generate the integrated emission spectrum, which is the experimental observable. For each electronic state, the emission spectrum is obtained by means of the Einstein coefficients with appropriate transition dipole moments and including the line broadening.

IV. RESULTS AND DISCUSSION

A. Pseudo-chirped pulses

We first discuss the case $M = 0$ in Eq. (1). Figure 2 presents the measured enhancement factor (EF), i.e., the ratio of the UV signal for the shaped pulse over the signal for the TL pulse, as a function of the phase shape parameters T and A . The maximal enhancement for cosine phase shapes with $M = 0$ is found to be 6.6, slightly larger than

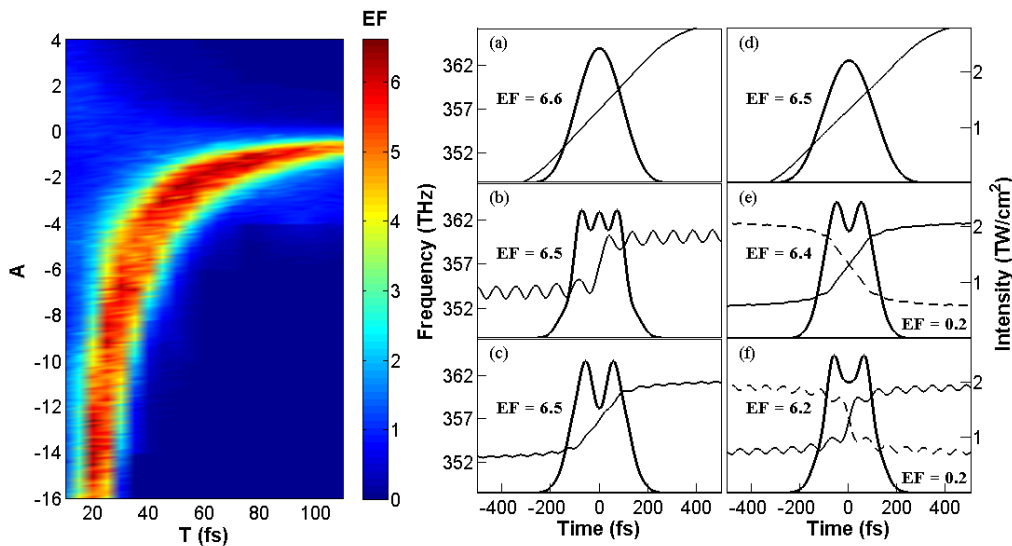


FIG. 2: Pseudo-chirped pulses ($M = 0$). Left: Experimental UV signal enhancement relative to the TL pulse (EF) as a function of T and A , cf. Eq. (1). Right: Examples of pseudo-chirped pulses yielding large enhancement. The intensity profile in time domain and the corresponding instantaneous frequency are plotted for: (a) $A = -12.6$, $T = 20$, (b) $A = -1.5$, $T = 75$, (c) $A = -2.3$, $T = 55$, (d) $A = -14$, $T = 20$, (e) solid line: $A = -2.4$, $T = 50$, dashed line: $A = 2.4$, $T = 50$, (f) solid line: $A = -1.7$, $T = 65$, dashed line: $A = 1.7$, $T = 65$. The corresponding values of the measured enhancement (EF) are also indicated.

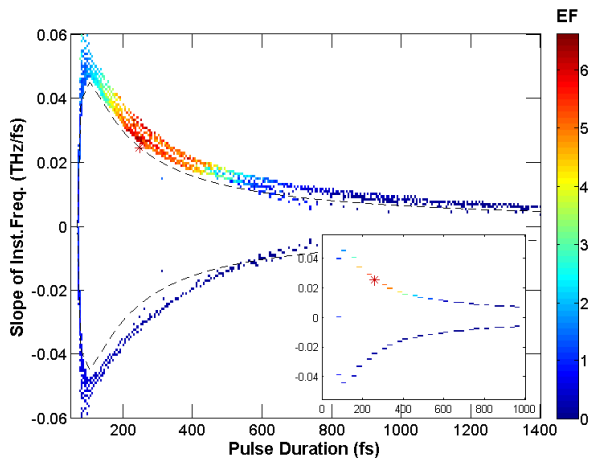


FIG. 3: Experimental UV signal enhancement (EF) as a function of instantaneous frequency slope and pulse duration (over the central part of the pulse) obtained for pseudo-chirped pulses. Inset: The corresponding map obtained for linearly chirped pulses. The dashed lines in the main map present the duration-slope combinations of the linearly chirped pulses (plotted to guide the eye).

the value for linearly chirped pulses. For positive values of A , we find suppression of the signal ($EF < 1$), similarly to the results for linearly chirped pulses with negative chirp [16]. The right-hand side of Fig. 2 displays examples of pseudo-chirped pulses which produce a large enhancement.

As explained above in Section II, pseudo-chirped pulses can be characterized by their duration and slope of the instantaneous frequency. Translating the spectral phase parameters A and T into these characteristics, Fig. 3 shows the enhancement factor as a function of pulse duration and temporal frequency slope. For comparison the inset shows the same map for linearly chirped pulses. Clearly, the range of pulse durations between approximately 200 fs and 400 fs and instantaneous frequency slopes between approximately 0.01 THz/fs and 0.04 THz/fs is optimal for achieving large enhancement factors, between 4.5 to 6.6. This finding is similar for both cosine phase-shaped pulses and linearly chirped pulses. For the highest enhancement factors, above 6.0, the optimal range of pulse durations and frequency slopes becomes narrower, with the corresponding values of 200–280 fs and 0.02–0.03 THz/fs, respectively. The dependence on the sign of the chirp, respectively slope of the instantaneous frequency, is reflected in the asymmetry of the map with respect to the axis of zero slope: For negative slope, suppression rather than enhancement ($EF < 1$) is found. The corresponding pulses are shown by dashed lines in Fig. 2(e),(f).

The results show that there is an extended set of chirped and pseudo-chirped pulses, with an extended range of pulse durations and frequency slopes, that lead to a large enhancement of the detected photoassociation yield. We associate the significant tolerance to the exact shape of the optimal pulse with the fact that, due to the initial thermal conditions, the photoassociation takes place from many different initial scattering states of the colliding atoms. Since each such initial state generally has a different energy and a slightly different wavefunction, the corresponding optimal pulse has a slightly different shape.

B. Asymmetric pulses with a sub-pulse structure

The second set of cosine phase-shaped pulses uses $M = 5.7$ in Eq. (1), leading to pulses with a sub-pulse structure. The experimental enhancement as a function of the parameters T and A is presented in the left-hand side of Fig. 4, together with six pulses producing a large enhancement over TL pulses in the right-hand side. The best asymmetric pulses result in higher enhancement factors than the best pseudo-chirped pulses. Here, the enhancement reaches an order of magnitude compared to TL pulses and is larger by about a factor of 1.5 compared to the pseudo-chirped pulses.

The duration of these pulses is more difficult to determine since they are divided into several sub-pulses. A better understanding of the advantage of these pulses over pseudo-chirped and linearly chirped pulses is obtained by inspecting the time delay between the sub-pulses. The optimal time delays between sub-pulses are identified by considering only those asymmetric pulses that produce enhancement factors larger than 8, see Fig. 5(a). For the delay between the first two sub-pulses (Δ_{12}), the optimum is found to be around 160 fs (red squares in Fig. 5(a)). The optimal delay between the second and third sub-pulse (Δ_{23}) is around 80 fs (blue squares in Fig. 5(a)), consistent with

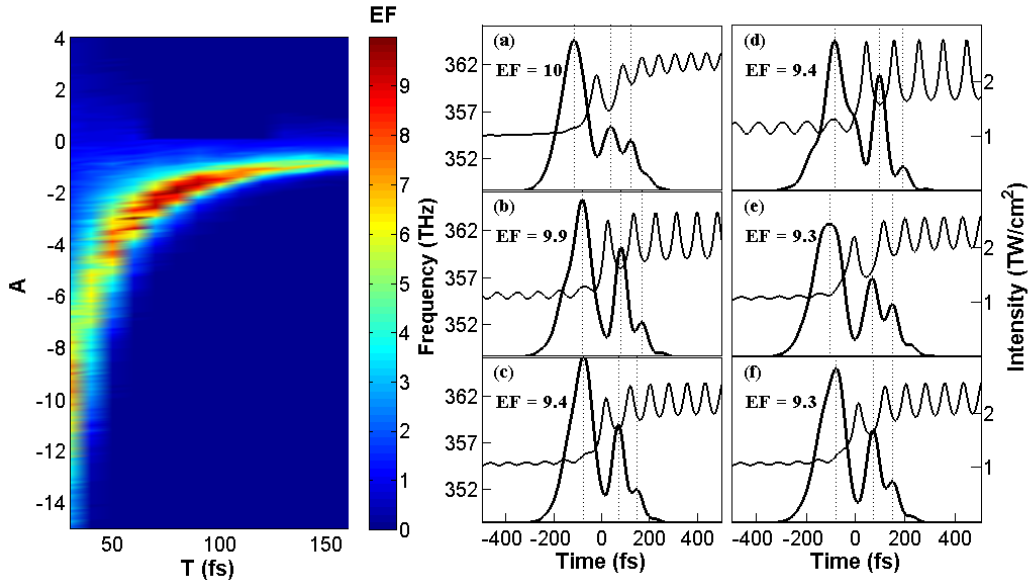


FIG. 4: Asymmetric pulses with a sub-pulse structure ($M = 5.7$). Left: UV signal enhancement (EF) as a function of T and A , cf. Eq. (1). Right: Examples of asymmetric pulses with a sub-pulse structure yielding large enhancement. The intensity profile in time domain and the corresponding instantaneous frequency are plotted for: (a) $A = -3$, $T = 60$, (b) $A = -2$, $T = 80$, (c) $A = -2.1$, $T = 70$, (d) $A = -1.7$, $T = 90$, (e) $A = -2.6$, $T = 70$, (f) $A = -2.3$, $T = 70$. The corresponding values of the measured enhancement (EF) are also indicated.

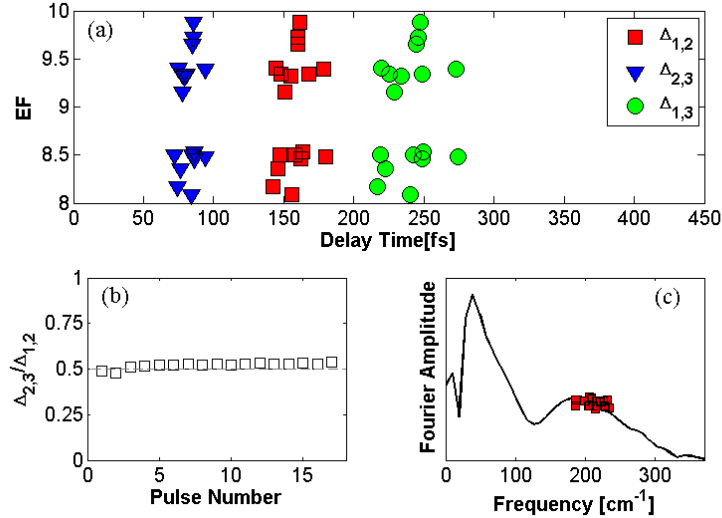


FIG. 5: (a) Enhancement factor vs time delays between sub-pulses: $\Delta_{1,2}$, i.e., delay between the first and second sub-pulse (red), $\Delta_{2,3}$ (blue), and $\Delta_{1,3}$ (green). (b) Time delay ratio $\Delta_{1,2}/\Delta_{2,3}$ for the data shown in panel (a). The average value corresponds to 0.52. (c) Spectrum of the quantum beat frequencies obtained in the pump-probe experiment [15] and frequencies corresponding to the delays shown in panel (a), which fit the vibrational peak of the quantum beat spectrum.

half of the first delay, see also Fig. 5(b). The delay between the first two sub-pulses corresponds to a frequency of $\sim 210 \text{ cm}^{-1}$. Using femtosecond pump-probe spectroscopy, we have earlier determined the quantum beat frequencies relevant in the photoassociation process [15]. The corresponding Fourier spectrum of the experimental transient pump-probe signal is compared in Figure 5(c) to the frequencies corresponding to the time delays of the asymmetric pulses. The delay between the first two sub-pulses (red squares) is found to fit the vibrational part of the pump-probe signal. The delay Δ_{13} between the first and third sub-pulse provides a rough estimate of the overall pulse

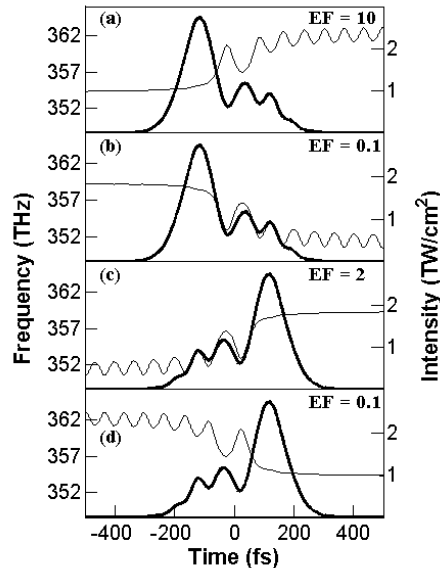


FIG. 6: Comparison of asymmetric pulses with a sub-pulse structure that have related pulse shape, obtained by different phase shape parameters (A , T , $M = \pm 5.7$), and their experimental EF values. Panels (a) and (b), respectively (c) and (d) compare pulses with the same temporal intensity profile but overall increasing vs. overall decreasing instantaneous frequency. Additionally, the relative intensity between the sub-pulses is compared between (a), (b) on one hand and (c), (d) on the other. (a) $A = -3$, $T = 60$, $M = 5.7$, (b) $A = 3$, $T = -60$, $M = 5.7$, (c) $A = -3$, $T = 60$, $M = -5.7$, (d) $A = 3$, $T = 60$, $M = 5.7$.

duration. For the well performing asymmetric pulses of Fig. 5(a), Δ_{13} is found to be in the range of 220 fs to 275 fs. This is in good agreement with the optimal pulse durations of the well performing pseudo-chirped pulses reported in Sec. IV A.

All well performing asymmetric pulses, cf. Fig. 5(a) and examples in Fig. 4, have a first sub-pulse that is of higher intensity and longer duration than the subsequent sub-pulses. These pulses also display an overall increasing instantaneous frequency where the onset of the increase is located in the second part of the first sub-pulse. The role of delay and instantaneous frequency is further analyzed in Fig. 6 which displays four pulses together with the enhancement that they yield. Comparison of panels (a) and (b), respectively (c) and (d), which show pulses with the same temporal intensity profile but overall increasing vs. overall decreasing instantaneous frequency, confirm the earlier observation of a clear advantage of increasing compared to decreasing instantaneous frequency: An overall increasing (decreasing) instantaneous frequency results in enhancement (suppression) of the UV signal. Figure 6 also allows to examine the role of relative intensity between the sub-pulses. Comparing, for example, panels (a) and (c) which both feature an overall increasing instantaneous frequency but differ in the increase vs decrease of the sub-pulse peak amplitudes, reveal the advantage of a strong first sub-pulse: The enhancement in panel (a) is larger by a factor of 5 compared to (c).

Let us summarize the features of asymmetric pulses that are particularly advantageous for enhancing the observed UV signal: (i) a stronger and longer first sub-pulse, (ii) an overall increasing instantaneous frequency which starts to increase in the second part of the first sub-pulse, (iii) an optimal sub-pulse delay Δ_{12} fitting exactly the $(1)^1\Pi_g$ vibrational period, and (iv) an optimal sub-pulse delay Δ_{23} fitting half the $(1)^1\Pi_g$ vibrational period. These findings suggest the following interpretation: The first sub-pulse creates a $(1)^1\Pi_g$ vibrational wavepacket, most likely at the right turning point, via free-to-bound two-photon photoassociation transitions. The non-resonant nature of these transitions requires a strong and temporally wide sub-pulse. In the second part of the first sub-pulse, the frequency starts to increase such that, after half a vibrational period, when the wavepacket has reached the left turning point, part of the amplitude is efficiently transferred into lower vibrational levels of the $(1)^1\Pi_g$ state by resonant Raman transitions via higher electronically excited states. These Raman transitions are favored by an instantaneous frequency increase [16]. Then, after another half vibrational period, i.e., one vibrational period after the photoassociation transition, the wavepacket has reached again the right turning point. This coincides with the peak amplitude of the second sub-pulse, i.e., with Δ_{12} , such that another part of the wavepacket, larger than before, is efficiently and coherently excited into lower $(1)^1\Pi_g$ vibrational levels via up-chirped Raman transitions. Last, after one more half vibrational period (Δ_{23}), the wavepacket is again at the left turning point, where the third sub-pulse drives another coherent Raman transition into lower $(1)^1\Pi_g$ vibrational levels. As we have previously shown and discussed [16], the

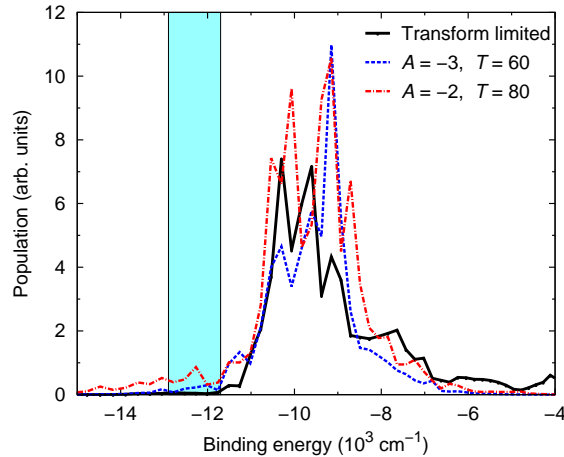


FIG. 7: Final distribution of vibrational levels in intermediate $(1)^1\Pi_g$ state for two optimal pulses compared with a TL pulse. The shaded area shows the band which can be transferred by a one-photon transition to the UV emission window below the $^1S + ^1P$ atomic threshold.

coherent enhancement of population in the lower vibrational levels of the $(1)^1\Pi_g$ state is directly reflected in the final population of the observed UV emitting band, which is accessed from the former by a weak one-photon transition.

We now compare these experimental findings to simulation results. For the two most efficient pulses, shown in Fig. 4(a) and (b), with experimental EF of 10 and 9.9, the theoretically obtained enhancement amounts to 6.8 and 18.3, respectively. Qualitatively, this confirms the strong enhancement of the UV signal for phase-shaped pulses compared to the TL pulse. In particular, the largest theoretically found enhancement for cosine phase-shaped pulses is also larger than the maximum enhancement obtained with linearly chirped pulses. However, due to the sensitivity of the dynamics on the details of the electronic structure data, as discussed in Ref. [16], it would be very challenging to reproduce the exact values for the experimental enhancement factors. In particular, the maximum enhancement was found for larger chirp rates in the calculations than in experiment [16]. Moreover, the agreement between experimental and theoretical results for the vibrational spectra of the pump-probe transients was satisfactory but not perfect [15]. A pulse which is experimentally found to maximally exploit the vibrational dynamics will therefore not necessarily be the best performing pulse in the calculations where the vibrational dynamics is slightly different.

Figure 7 presents the final vibrational distribution in the intermediate $(1)^1\Pi_g$ state. Assuming that the final probe transition from the $(1)^1\Pi_g$ state into the UV emitting states can be treated perturbatively, it is the $(1)^1\Pi_g$ vibrational distribution that reveals the control mechanism [16]. For example, linearly chirped pulses were found to up-, respectively down-shift the $(1)^1\Pi_g$ vibrational distribution by Raman transitions between the $(1)^1\Pi_g$ and higher lying electronic states. This modifies in particular the population that is transferred by the probe photon, marked by the shaded area in Fig. 7, into the band of rovibrational levels in the *ungerade*-states that produce the measured UV emission [16]. Inspection of Fig. 7 clearly shows that cosine phase-shaped pulses tend to transfer more population to the most deeply bound levels in the $(1)^1\Pi_g$ band than the TL pulse. Thus, the Raman cycling process discussed in Ref. [16] is efficient also in case of the new family of asymmetric sub-pulse structured pulses.

V. CONCLUSIONS

Control of binary reactions is one of the most difficult tasks of coherent control. The first step of two-photon Franck Condon filtering purifies the initial thermal state and thus sets the stage for control. The target task in the present study was to control the generation of bound Mg_2 molecules in the band of vibrational levels of *ungerade* states just below the $^1P + ^1S$ dissociation threshold. Population in this band is detected experimentally by its transition back to the ground state which results in emission of UV light. Once a target is set we can decipher the interference control mechanism optimizing this task. The present work demonstrates the power of a constructive approach based on cosine spectral phase patterns. The constructive approach limits the number of control parameters and therefore enables a rational approach to optimization. We are able to identify two control mechanisms—electronic and vibrational.

The electronic component employs the full manifold of electronic surfaces generating interference pathways which are Raman-like. The electronic control mechanism enhances population in intermediate levels which are transferred to the target band by a weak final probe step. In addition, we identify by the time delay between sub-pulses a vibrational mechanism which employs the interference between a direct excitation and a delayed excitation. We find a relatively high tolerance to the exact shape of the optimal pulse for enhancing the detected UV signal. We associate it with the highly thermal character of the initial atomic ensemble which is held at a temperature of 1000 K.

The roadmap explored in the control of strong-field photoassociation of magnesium dimers opens the door to more complex binary reactions. The main lesson learnt with Mg_2 can be summarized as follows: Bond making requires a purification step which implies that only a relatively small number of reactants can be addressed. It is then crucial to employ shaped femtosecond pulses of high intensity for maximizing this number as much as possible and, at the same time, coherently controlling the excitation dynamics to a very high degree. On the other hand, it is also crucial to ensure an almost background-free detection of the photoassociated molecules. It was achieved here by the choice of closed-shell reactants and a non-resonant multiphoton photoassociation transition. This insight provides a blueprint for studying e.g. triatomic reactions which would allow for stable reaction products and two possible reaction outcomes. The basic scenario of utilizing interference in time domain for the coherent control of binary reactions has thus been established. Thirty years after conception of the idea, perspectives for the coherent control of binary reactions finally look bright.

Acknowledgments

This research was supported by The Israel Science Foundation (Grant No. 1450/10) and the Alexander von Humboldt Foundation (WS).

-
- [1] D. J. Tannor, R. Kosloff, and S. A. Rice, *J. Chem. Phys.* **85**, 5805 (1986).
 - [2] P. Brumer and M. Shapiro, *Principles and Applications of the Quantum Control of Molecular Processes* (Wiley Interscience, 2003).
 - [3] M. Dantus and V. V. Lozovoy, *Chem. Rev.* **104**, 1813 (2004).
 - [4] A. M. Weiner, *Rev. Sci. Instrum.* **71**, 1929 (2000).
 - [5] D. Tannor and S. A. Rice, *J. Chem. Phys.* **83**, 5013 (1985).
 - [6] J. L. Krause, M. Shapiro, and P. Brumer, *J. Chem. Phys.* **92**, 1126 (1990).
 - [7] T. Seideman, J. L. Krause, and M. Shapiro, *Chem. Phys. Lett.* **173**, 169 (1990), ISSN 0009-2614.
 - [8] M. Shapiro and P. Brumer, *Phys. Rev. Lett.* **77**, 2574 (1996).
 - [9] A. Abrashkevich, M. Shapiro, and P. Brumer, *Phys. Rev. Lett.* **81**, 3789 (1998).
 - [10] V. Zeman, M. Shapiro, and P. Brumer, *Phys. Rev. Lett.* **92**, 133204 (2004).
 - [11] A. B. Henson, S. Gersten, Y. Shagam, J. Narevicius, and E. Narevicius, *Science* **338**, 234 (2012).
 - [12] F. H. J. Hall and S. Willitsch, *Phys. Rev. Lett.* **109**, 233202 (2012).
 - [13] S. Ospelkaus, K.-K. Ni, D. Wang, M. H. G. de Miranda, B. Neyenhuis, G. Qumner, P. S. Julienne, J. L. Bohn, D. S. Jin, and J. Ye, *Science* **327**, 853 (2010).
 - [14] R. Kosloff, S. Rice, P. Gaspard, S. Tersigni, and D. Tannor, *Chem. Phys.* **139**, 201 (1989).
 - [15] L. Rybak, S. Amaran, L. Levin, M. Tomza, R. Moszynski, R. Kosloff, C. P. Koch, and Z. Amitay, *Phys. Rev. Lett.* **107**, 273001 (2011).
 - [16] L. Levin, W. Skomorowski, L. Rybak, R. Kosloff, C. P. Koch, and Z. Amitay, *Phys. Rev. Lett.* **114**, in press (2015), arXiv:1411.1542.
 - [17] S. Amaran, R. Kosloff, M. Tomza, W. Skomorowski, F. Pawłowski, R. Moszynski, L. Rybak, L. Levin, Z. Amitay, J. M. Berglund, et al., *J. Chem. Phys.* **139**, 164124 (2013).
 - [18] G. D. Gillen, M. A. Walker, and L. D. Van Woerkom, *Phys. Rev. A* **64**, 043413 (2001).
 - [19] P. J. Ziemann and A. W. Castleman Jr., *Z. Phys. D* **20**, 97 (1991).
 - [20] A. M. Weiner, *Rev. Sci. Instrum.* **71**, 1929 (2000).
 - [21] L. Rybak, Z. Amitay, S. Amaran, R. Kosloff, M. Tomza, R. Moszynski, and C. P. Koch, *Faraday Disc.* **153**, 383 (2011).
 - [22] R. Kosloff, *Annu. Rev. Phys. Chem.* **45**, 145 (1994).